Scilight

Photochemistry and Spectroscopy
https://www.sciltp.com/journals/ps

Article

Check for updates

Raman and ATR-FTIR Spectroscopic Profiling Coupled with Gene Expression to Monitor Physiopathological Dynamics in 3D HepG2 Liver Cancer Spheroids †

Enza Fazio [1,*], Carmelo Corsaro [1], Vincenza Crupi [1], Sabrina Conoci [2,3,4], Fortunato Neri [1] and Maria Giovanna Rizzo [2]

[1] Department of Mathematical and Computer Sciences, Physical Sciences and Earth Sciences (MIFT), University of Messina, Viale F. Stagno d'Alcontres, 31, 98166 Messina, Italy
[2] Department of Chemical, Biological, Pharmaceutical and Environmental Sciences (CHIBIOFARAM), University of Messina, Viale F. Stagno d'Alcontres, 31, 98166 Messina, Italy
[3] CNR-DSFTM, URT LabSens Beyond Nano Messina, Viale F. Stagno d'Alcontres, 31, 98166 Messina, Italy
[4] Department of Chemistry G. Ciamician, University of Bologna, Via Francesco Selmi 2, 40126 Bologna, Italy
* Correspondence: enfazio@unime.it
† This article is dedicated to Prof. Giuseppe Zerbi in recognition of his outstanding scientific contributions to Spectroscopy.

How To Cite: Fazio, E.; Corsaro, C.; Crupi, V.; et al. Raman and ATR-FTIR Spectroscopic Profiling Coupled with Gene Expression to Monitor Physiopathological Dynamics in 3D HepG2 Liver Cancer Spheroids. *Photochemistry and Spectroscopy* **2026**, *2*(2), 2. https://doi.org/10.53941/ps.2026.100013

Received: 30 October 2025
Revised: 29 December 2025
Accepted: 21 January 2026
Published: 13 April 2026

Abstract: The integration of micro-Raman and ATR-FTIR spectroscopies with qRT-PCR gene expression analysis provides a multimodal strategy for profiling three-dimensional hepatocellular carcinoma (HCC) spheroids. This approach enables temporal monitoring of tumor growth, metabolic adaptation, and microenvironmental remodeling. Gene expression revealed an early proliferative phase (*PCNA*, *KI-67*, *AFP*), followed by activation of hypoxia- and stress-associated pathways (*HIF1α*, *SLC2A1/GLUT1*, *LDHA*) and modulation of extracellular matrix (ECM) components (*SPARC*, *FN1*) alongside the pro-apoptotic regulator *BBC3*. In parallel, Raman and ATR-FTIR spectroscopies non-invasively detected biochemical variations related to oxidative stress, lipid accumulation, apoptosis, and ECM remodeling. The observed correlations between spectral signatures and molecular markers demonstrate that these label-free spectroscopic fingerprints are reliable indicators of physiopathological processes. Our research integrates molecular spectroscopy with transcriptomics to provide an innovative and comprehensive approach for a quick and first evidence of tumor progression.

Keywords: micro-Raman; infrared spectroscopy; qRT-PCR; hepatocellular carcinoma; hypoxia; apoptosis; oxidative stress; extracellular matrix remodeling; tumor microenvironment; physiopathological processes

1. Introduction

The study of cellular dynamics within three-dimensional (3D) biological models has become increasingly important for advancing our understanding of complex physiological and pathological processes, particularly in oncology. Unlike traditional two-dimensional (2D) cell cultures, which grow cells on flat, rigid substrates and fail to replicate the metabolic plasticity and microenvironmental remodeling of hepatocellular carcinoma (HCC), 3D spheroid models more accurately recreate the spatial architecture and microenvironment of living tissues [1–3]. These models simulate extracellular matrix (ECM) interactions, intercellular communication, and critical gradients of oxygen, nutrients, and metabolites, thereby enhancing preclinical relevance for drug development [4–9].

HepG2 cells, a robust and widely used human HCC cell line, form stable, reproducible spheroids under scaffold-free conditions, capturing key hallmarks of disease progression such as hypoxia-induced metabolic shifts, oxidative stress, hypoxia-inducible factor stabilization, and ECM reorganization [10–13]. These gradients spontaneously drive tumor adaptation in 3D, unlike static 2D monolayers, providing a reliable platform for longitudinal multimodal molecular and spectroscopic studies. Tracking HepG2 spheroids over weeks reveals the dynamic evolution of these traits, offering a physiologically accurate view of HCC advancement that emphasizes adaptive responses beyond mere cellular senescence or survival metrics [1–3].

Within this context, vibrational spectroscopic techniques such as Raman and Attenuated Total Reflectance Fourier-Transform Infrared (ATR-FTIR) spectroscopy have emerged as powerful tools for probing the molecular composition of biological samples [4]. Raman spectroscopy leverages inelastic scattering of monochromatic light to detect specific molecular vibrations, enabling real-time, label-free, and non-destructive monitoring of biomolecular changes including proteins, lipids, and nucleic acids. This capability allows for dynamic tracking of cellular processes such as maturation, differentiation, metabolic shifts, and stress responses [5]. Furthermore, ATR-FTIR spectroscopy identifies characteristic vibrational modes across molecular functional groups, providing sensitive detection of subtle biochemical changes in complex biological matrices [6,10]. Together, these spectroscopies yield a comprehensive molecular fingerprint, capturing diverse facets of cell biology that might remain elusive when using conventional biochemical or imaging techniques alone [11,12].

A key strength of this study lies in the deliberate integration of Raman and ATR-FTIR spectral data with gene expression profiling to comprehensively characterize the 3D HepG2 spheroid model, which mimics carcinoma progression. While spectroscopic methods excel at delivering holistic, non-invasive snapshots of phenotypic and metabolic alterations, such as lipid peroxidation, protein secondary structure shifts, and nucleic acid conformational changes, gene expression analysis unveils the underlying regulatory networks driving these observations, including hypoxia-responsive genes (e.g., *HIF1α*), metabolic enzymes (e.g., *LDHA*), and ECM remodelers. This multimodal approach is essential, as spectra alone may detect downstream biochemical signatures without revealing causal genetic mechanisms, and transcriptomics in isolation often overlooks post-transcriptional or microenvironmental influences captured by vibrations. By correlating these datasets, we achieve a synergistic understanding of adaptive tumor dynamics in the 3D model, surpassing the limitations of unimodal analyses and providing unprecedented insights into tumor dynamics for targeted therapeutic development.

2. Experimental Section

2.1. D Human Hepatocellular Carcinoma Model Generation

The experiments were performed using human hepatocellular carcinoma HepG2 cells (HepG2; ATCC, HB-8065, Manassas, VA, USA), which were selected for their ability to reproducibly generate scaffold-free 3D spheroids and to maintain stable tumor-like phenotypic and metabolic features over prolonged culture periods. HepG2 cells were maintained in 75 cm^2 culture flasks containing high glucose DMEM medium (D6429; Sigma, St. Louis, MO, USA) supplemented with 2.5 mM L-glutamine (G7513, Merck LifeScience S.r.l., Milan, Italy), 10% Fetal Bovine Serum (F7524, FBS, Merck Life Science S.r.l., Milan, Italy), 1% penicillin/streptomycin/amphotericin (A5955, Merck Life Science S.r.l., Milan, Italy), and incubated in a humidified atmosphere containing 5% CO_2 at 37 °C. No hypoxic chambers, oxygen-controlled incubators, or chemical hypoxia inducers were used (see Ref.s [13,14] for more details). The 3D spheroid models were created seeded as single-cell suspensions in 96-well ultra-low-adhesion round-bottom plates (174,927, Thermo Scientific, Waltham, MA, USA) at defined densities of 5000 cells/well in a final volume of 100 μL/well that is a condition previously optimized to ensure morphological stability, reproducible growth, and sustained viability during long-term culture. Spheroids were monitored by using several biological and spectroscopic approaches at 1, 2, and 4 weeks.

To investigate the morphological changes during the cell proliferation and differentiation stages, some optical images were acquired by using a 3D confocal microscope (Figure 1). The adopted digital microscope (Hirox-HRX-01 model by Simitecno s.r.l., Rome, Italy) uses a combination of high-resolution optics and is designed for 2D/3D inspections of objects of any size, utilizing motorized telecentric lenses and confocal sensors for submicrometer measurements.

3D optical images have been generated by acquiring a series of focal planes along the Z-axis, which are processed to create a three-dimensional topographic map of the surface. The Hirox microscope is ideal for analyzing biological samples, as it allows for easy understanding of complex shapes or surfaces, allowing for subsequent observations and comparisons. Figure 1 depicts 3D and 2D optical images of the investigated spheroids, so monitoring growth and morphological organization over time. Our 3D model captures essential features of HCC progression and provides a reliable tool for studying tumor dynamics. At t = 0 (24 h after the

incubation), cell surface is flat with slight protrusions. After the first week, the formation of a spheroidal structure measuring approximately 550 μm, typical of 3D cell cultivation, is evident, with the possible appearance of a central circular structure. After two and four weeks, the spheroids are characterized by an irregular morphology, which can be approximated to a circumference with a diameter of about 800 μm, suggesting a differentiation in the cellular organization of the various components (nucleus, cell membrane, etc.). The optical evidences are in good agreement with the expected HepG2 3D model time-dependent maturation characterized by progressive spheroid growth, increased structural compactness, and metabolic adaptation over the culture period. Spheroids displayed a reproducible size evolution, reaching diameters compatible with the establishment of physiological gradients of oxygen and nutrients typical of three-dimensional tumor models: over time, the model transitioned from an early proliferative phase toward a more stabilized state, consistent with reduced proliferation and enhanced extracellular matrix remodeling. This maturation process was associated with changes in cellular organization and ECM-related features, in agreement with previously validated scaffold-free HepG2 spheroid models [15,16].

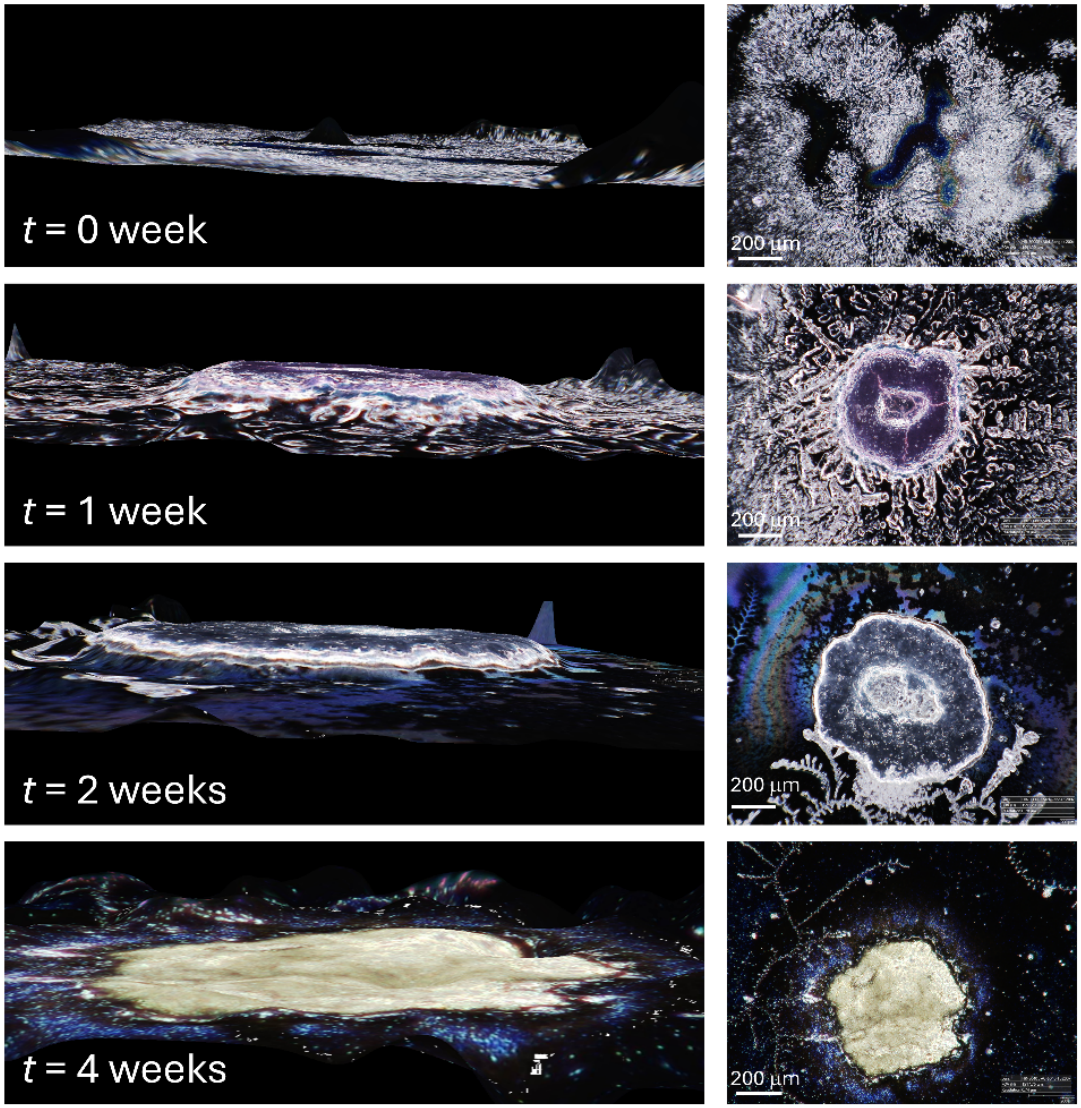

Figure 1. 3D and 2D optical inspection of the investigated spheroids. Optical images were acquired with a 200x objective and on a scale of 200 μm.

2.2. Micro-Raman and ATR-FTIR Spectroscopies

Micro-Raman and ATR-FTIR spectroscopies were employed to detect specific biomarkers of carcinoma and to follow the biochemical composition and HepG2 cellular response over time, allowing a noninvasive monitoring of metabolic states by investigating specific molecular vibrations. For FT-IR and Raman measurements, spheroids were fixed on CaF_2 substrates (selected for their excellent transmission across the UV, visible, and infrared regions) using 4% formalin for 20 min at room temperature. After fixation, samples were washed twice in ultrapure water and air-dried at room temperature. Spheroids were generated from an initial cell density of 5×10^4 cells/mL

and monitored at 1, 2, and 4 weeks. All measurements were performed on three independent experiments with triplicate samples to ensure reproducibility. The drying conditions were ambient air at room temperature. No sectioning of spheroids was performed before measurements. Thus, spheroids were analyzed as intact three-dimensional structures without sectioning. The size of spheroids at each time point was consistent with previously published data [13,14] and estimated by analyzing optical images (Figure 1).

ATR-FTIR spectra were collected in the 650–4000 cm^{-1} wavenumber range, by using a Perkin Elmer (Bridgeport, CT, USA) Spectrum 100 spectrometer employed with a Nernst lamp as source, an MCT (Mercury Cadmium Telluride) detector with a resolution of 2 cm^{-1}. The spectrometer mounted a single-reflection Attenuated Total Reflectance (ATR) accessory, the Universal ATR (UATR) with a diamond crystal for robust, reproducible sampling. The ATR uses a single-reflection diamond crystal top-plate, which provides one internal reflection at an angle of incidence typically around 45° (standard for such single-reflection design), ensuring shallow penetration depth of about 1–3 μm. Penetration depth is driven by the diamond's high refractive index ($n \approx 2.4$) and the incidence angle, minimizing refractive index effects on spectral interpretation. The samples have been put in a good physical contact with the crystal by a controlled pressure arm, ensuring consistent and reproducible contact, which improves spectral quality and reliability. Post-measurement, the diamond crystal surface was cleaned sequentially with pure ethanol (99.5% purchased by Merck) using a lint-free wipe, followed by a water rinse and drying with compressed nitrogen to prevent residue buildup and ensure reproducibility. All measurements have been performed at room temperature on several areas of the same sample so obtaining multiple spectra for each zone. ATR-FTIR profiles have been collected after seedings the cell specimen on a CaF_2 substrate. The spectra of the cells at $t = 0$ (corresponding to the first day i.e., 24 h after incubation) as well as the spectra of the samples after 1, 2 and 4 weeks from cells incubation, were processed after acquisition using polynomial baseline correction and normalized to their respective total integrated areas.

Micro-Raman spectra were recorded using a Horiba XploRa spectrometer. HepG2 3D samples were analyzed in a near-liquid state to capture Raman features more representative of native liquid conditions. Raman signals in this state (data not shown) were relatively weak, despite spectral similarities to dried samples. Strong Raman signals, in the dried state, were obtained under the following settings: 532 nm laser excitation, laser power below 1 mW, laser spot size of 1–2 μm, integration times ranging from 30 to 60 s and, 1 to 3 accumulations to optimize the signal-to-noise ratio. Photodamage controls during Raman spectroscopy were implemented by optimizing laser power and exposure time. To minimize sample degradation, the laser power was fixed lower than 1 mW and the exposure time was limited to 30 s per acquisition. These values were chosen based on preliminary tests that monitored spectral stability over time. The 3D model allowed us to simulate realistic cellular conditions, and repeated spectra were acquired in each session to confirm the absence of alterations indicative of degradation. These parameters ensured reproducible measurements and preserved the sample's integrity throughout the experiment. The backscattered Raman light was dispersed using a 600 lines/mm grating and detected by a Deep Cooled CCD camera maintained at −60 °C. Daily calibration of the system was performed using the 521 cm^{-1} crystalline silicon line for spectral alignment. Background spectra were acquired on CaF_2 substrate surfaces, and all spectra were normalized to their respective integration times. Moreover, a linear baseline correction was employed before normalization to the corresponding total integrated area. To assess intracellular variability, Raman measurements were taken on multiple points through the sample surface. Environmental conditions including temperature, humidity, and laser power stability were continuously monitored and controlled due to their potential influence on Raman spectral quality.

2.3. Gene Expression

To assess gene expression levels during the progression of the 3D model, quantitative real-time PCR (qRT-PCR) was employed to first evaluate the genes *PCNA*, *KI-67*, *AFP*, *HIF1α*, and *BBC3*. Total RNA was isolated from samples cultured for 1, 2, and 4 weeks using TRIzol reagent (Invitrogen, Carlsbad, CA, USA) according to the manufacturer's instructions. The concentration of RNA was measured using an ND-1000 UV spectrophotometer (NanoDrop, Wilmington, DE). qRT-PCR reactions were prepared in a total volume of 20 μL, consisting of 1 μL cDNA, 0.5 μM of each primer, and 10 μL of SsoAdvanced Universal SYBR Green Supermix (2X) (Bio-Rad Laboratories, Hercules, CA, USA). Amplification was carried out on a 7500 Fast Real-Time PCR System, with melting curve analysis performed using the default settings of the instrument. *GAPDH* was used as the reference housekeeping gene for normalization, selected for its stable expression across the different experimental conditions and time points analyzed. Gene expression levels were calculated using the $2^{-\Delta\Delta Ct}$ method and are presented as fold changes relative to expression at day 1, after normalization to *GAPDH* [17–21]. Then, the expression patterns of the *SLC2A1* gene (encoding GLUT1) and *LDHA*, both associated with metabolic adaptation to hypoxia,

were examined. Additionally, to evaluate remodeling of the extracellular matrix (ECM), the levels of *SPARC* (Secreted Protein Acidic and Cysteine Rich) and *FN1* (Fibronectin 1) were analyzed. These markers were quantified through qRT-PCR at multiple time points, 1, 2, and 4 weeks in culture, compared to the baseline measurement taken at 24 h (day 1).

Hierarchical clustering analysis was conducted to identify groups of genes exhibiting distinct regulatory patterns throughout the experimental progression of the 3D model. Euclidean distance was used as the dissimilarity measure, and clusters were generated using the average linkage method. The clustering is then able to reveal distinct expression modules, distinguishing genes with synchronized activation patterns from those that follow independent or inverse trends. Finally, Raman and ATR-FTIR data have been correlated with the different components of gene expressions. The *r* values reported for each dashed line (in the figures of the following sections) correspond to the Pearson's correlation coefficient, able to quantify the linear relationship between the considered variables. Values close to 1 indicate a strong positive correlation whereas those close to -1 a strong negative correlation.

3. Results

3.1. Gene Expression

The time-course examination of gene expression in the 3D HepG2 cell model highlights distinct stages of cellular function evolving over the culture period, as reported in Figure 2a,b. In detail, Figure 2a displays the temporal evolution of gene expression levels for all analyzed genes through weeks 1, 2, and 4. Each curve represents a single gene, with values corresponding to the mean expression (±SD), showing differential temporal regulation of transcriptional responses. Specifically, genes with strong but variable induction versus those showing stable expression patterns are well identified through the bubble plot shown in Figure 2b. Each bubble corresponds to a gene–week pair: the colour encodes the mean expression level, while the bubble size represents the associated standard deviation. It emerges that both *PCNA* and *KI-67* expressions show the highest value at 1 week, sharply decreasing after 2 weeks and with a level off at 4 weeks. The differentiation marker *AFP* shows a similar trend but with a less pronounced variation. Instead, the response to hypoxic conditions, *HIF1α* levels, after a first increase, remained relatively constant throughout the time intervals measured, indicating cellular adaptation to the low-oxygen environment. Concerning the pro-apoptotic marker *BBC3*, it showed small overall changes with a first increase from 1 to 2 weeks followed by a small decrease/stabilization at 4 weeks. These temporal gene expression patterns depict a well-defined progression from an initial proliferative phase toward differentiation, followed by a stabilization period. This sequence highlights the 3D HepG2 model's capacity to effectively mimic crucial physiological adaptations occurring within the tumor microenvironment over time. In addition, *LDHA* expression showed an increase with time. Examining the roles of both *GLUT1* and *LDHA* simultaneously allows for a thorough insight into how glycolysis is regulated and how metabolic shifts occur in various diseases. *GLUT1* governs the cellular uptake of glucose, serving as the entry point to the pathway, whereas *LDHA* encodes lactate dehydrogenase A, responsible for directing pyruvate metabolism downstream. Together, these genes modulate critical processes such as cellular energy generation, biosynthetic activities, and adaptation mechanisms under low oxygen or altered nutrient conditions. The coordinated rise of *GLUT1* and *LDHA* indicates a shift towards aerobic glycolysis (Warburg effect), reflecting the bioenergetic adaptation of cancer cells to hypoxic stress. Consequently, investigating the expression and function of both genes is essential for understanding cancer metabolism and other pathological states, offering potential targets for therapy or markers to track disease progression and treatment efficacy.

Then, we focused on analyzing *SPARC* and *FN1* due to their crucial functions in modulating extracellular matrix (ECM) interactions, which in turn influence cellular metabolism and the glycolytic pathway. Specifically, *SPARC* encodes a cysteine-rich acidic protein that is part of the ECM protein family, playing an important role in ECM organization and facilitating tumor invasion. The expression profile of *SPARC* displayed a progressive increase, starting from 1.50 ± 0.50-fold at week 1, approaching its highest level at week 4 (3.50 ± 0.30 relative to day 1). This pattern of upregulation suggests ongoing ECM remodeling throughout spheroid maturation. In contrast, *FN1* codes for an ECM glycoprotein that is vital for cell adhesion, migration, and matrix remodeling, with prominent roles in processes such as wound healing and metastasis formation. Its expression showed an almost linear increase with time. Hence, both *SPARC* and *FN1* demonstrated a significant, time-dependent upregulation, showing their dynamic involvement in ECM remodeling during spheroid maturation. The progressive upregulation of *SPARC* and *FN1* highlights the active remodeling of the ECM, a physiopathological hallmark of tumor progression that facilitates cell invasion and metastatic dissemination.

Ultimately, HepG2 3D model characterization highlights specific differentiation markers assessed in spheroids compared to 2D monolayers. Specifically, regarding the degree of maturation, HepG2-derived 3D spheroids exhibit time-dependent maturation, with reduced proliferation and enhanced metabolic competence

compared to 2D cultures. As reported below, FTIR analysis tracks chemical and structural changes from initial cell suspension through spheroid formation up to 4 weeks, showing progressive biochemical shifts indicative of maturing hepatocytes. Regarding ECM structure, immunofluorescence staining (not shown here but discussed in Ref. [13] reveals organized extracellular matrix (ECM) development in the 3D HCC model after 1 and 4 weeks of culture. ECM remodeling is driven by hypoxia-induced oxidative stress, with distinct structural evolution in HepG2 spheroids. This scaffold-free approach promotes cell-cell and cell-matrix interactions mimicking in vivo liver architecture. On the overall, the differentiation markers, including genes encoding hepatic functions, showed time-dependent deregulation in 3D cultures, indicating enhanced differentiation. Proliferation-related markers like *KI-67* (a cellular proliferation marker) and PCNA (proliferating cell nuclear antigen) revealed a strong decrease in proliferation linked to differentiation processes over time. Then, these findings, from flow cytometry and qPCR analyses on spheroids formed via the forced floating method (initial densities of 3000 or 6000 cells/spheroid, as detailed in Ref. [13], underscore the 3D model's shift toward a more physiologically relevant hepatic phenotype.

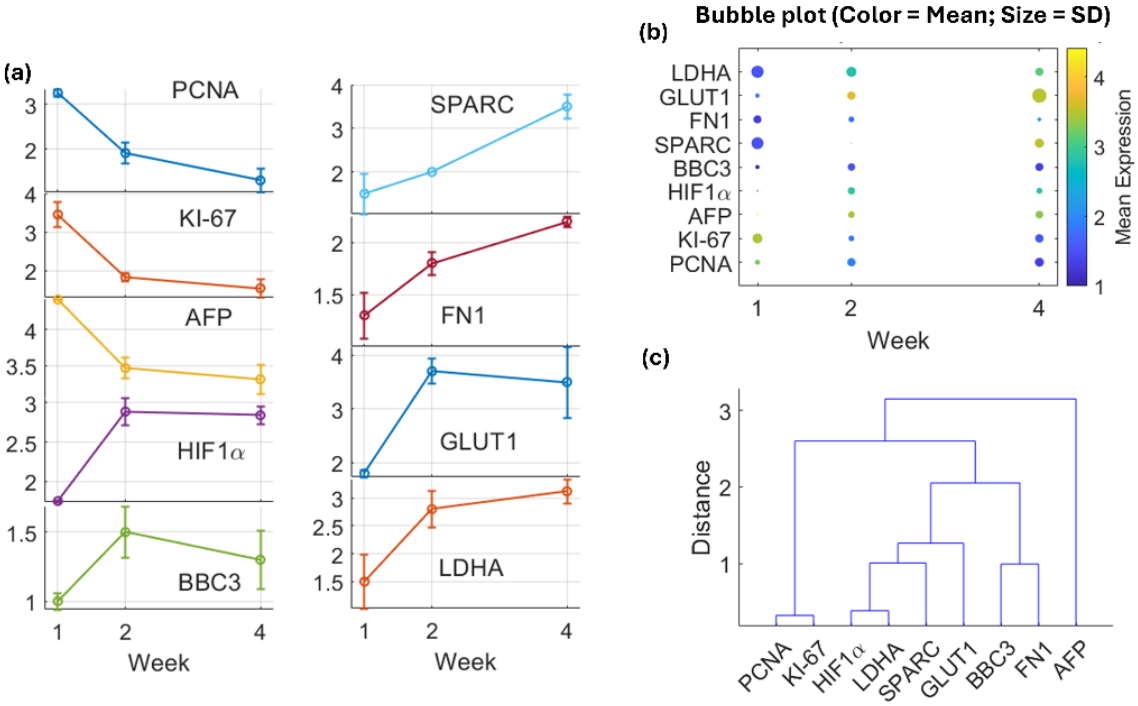

Figure 2. (**a**) Gene expression trend over time reporting the mean expression (±SD). (**b**) Bubble plot in which the colour encodes the mean expression level, while the bubble size represents the associated standard deviation. (**c**) Hierarchical dendrogram grouping genes based on the similarity of their expression profiles across time.

To group genes with similar expression profiles through time, a hierarchical clustering analysis (Figure 2c) was carried out. As expected, *PCNA* and *KI-67* cluster very closely, indicating nearly identical temporal behaviour, consistent with their common association with cell proliferation. *HIF1α* joins this cluster at a slightly higher distance, suggesting a related but partially distinct regulation pattern reflecting metabolic adaptation. A second cluster includes *LDHA, SPARC*, and *GLUT1*, which share intermediate distances, indicating coordinated upregulation linked to extracellular remodeling processes in agreement with the model evolution. Finally, *BBC3, FN1*, and especially *AFP* form a more distant branch, suggesting divergent transcriptional behaviour compared to the proliferative/metabolic group. Their higher linkage distance reflects less synchronized changes in expression across the observed weeks.

3.2. ATR-FTIR and Raman Analyses

Figure 3 shows ATR-FTIR spectra of the 3D hepatocellular carcinoma (HCC) model at 1, 2, 4 weeks as well as at the $t = 0$ (24 h after the incubation). Regarding the observed peculiar ATR-FTIR features, the distinctive absorption bands centred at about 1080 cm^{-1} and 1230 cm^{-1}, correspond to symmetric and asymmetric phosphate (PO_2^-) stretching vibrations of nucleic acids, respectively [13]. Monitoring these bands provides insights into nuclear integrity and the progression of apoptosis, consistent with the increased apoptotic markers and reactive oxygen species (ROS) accumulation observed.

The bands centred at about 1400 and 1450 cm^{-1} ascribable to the symmetric bending deformation of methyl groups ($–CH_2$ and $–CH_3$) in the side chains of proteins or in lipids displays a general increasing trend supporting the occurrence of lipid accumulation and cellular differentiation typical of the suffering state due to hypoxic conditions [22]. These vibrations, part of the CH deformation region (typically 1350–1480 cm^{-1}), strengthen with higher lipid content, as seen in differentiating or suffering cells where membranes proliferate [23]. The contribution at 1400 cm^{-1} can be also due to the symmetric COO^- stretching, indicating the presence of carboxyl groups in ECM molecules, like glycosaminoglycans, or deprotonated amino acids in proteins, especially under altered pH or remodeling in hypoxic conditions. Alternative assignments include CH_2 twisting/wagging near 1450 cm^{-1} or amide III contributions (C-N stretch + N-H bend) from proteins around 1400 cm^{-1}, though lipid CH deformations dominate in spectra showing accumulation trends [24,25].

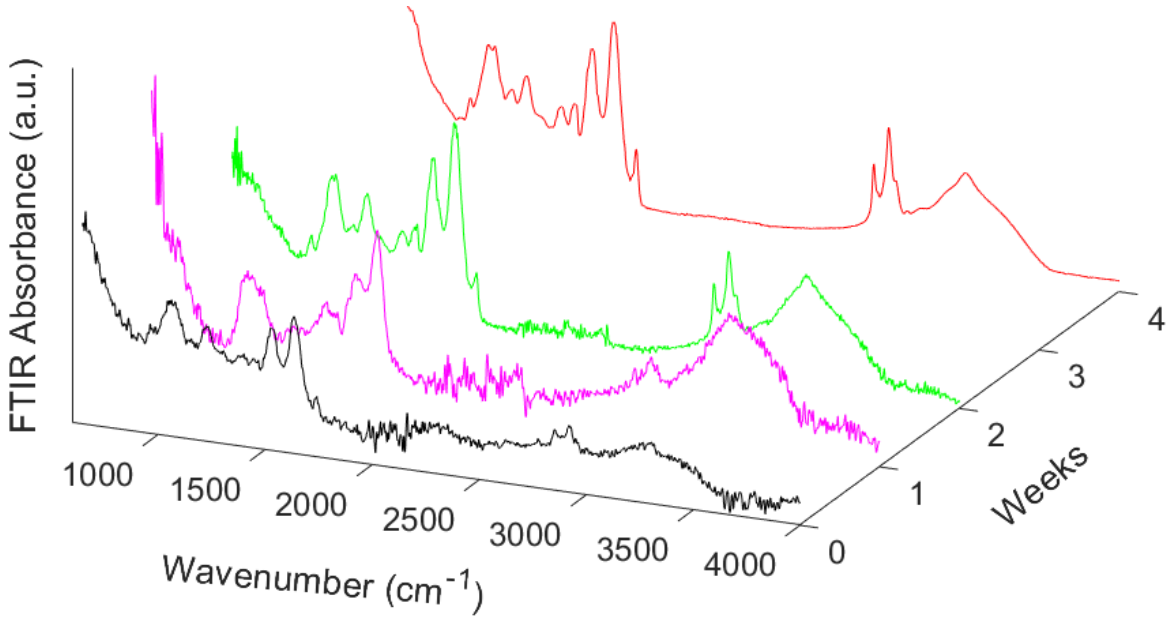

Figure 3. ATR-FTIR spectra of HepG2 3D model acquired at 1, 2, 4 weeks as well as at the t = 0 (24 h after the incubation).

The band at 1450 cm^{-1} shows a negative correlation with PCNA (Proliferating Cell Nuclear Antigen) and AFP (Alpha-fetoprotein) levels (Figure 4a). This suggests that, as lipid accumulation and cell differentiation increase (indicated by this band) the proliferation activity (PCNA) and AFP expression decrease, further supporting the cellular response to hypoxia [26,27]. Furthermore, the positive correlation with FN1, LDHA and BBC3 trend (Figure 4b) could imply a link between the biochemical composition captured by this ATR-FTIR band and cellular processes involving extracellular matrix remodeling (FN1) and metabolic adaptation to hypoxia (LDHA, a key enzyme in glycolysis, promoting the metabolic shift known as the "Warburg effect" in cancer cells, which supports rapid cell proliferation and resistance to cell death). Protein content and secondary structural elements are evidenced by the presence of amide bands, particularly Amide I (approximately at 1650 cm^{-1}, mainly due to C=O stretching), Amide II (at around 1560 cm^{-1}) and Amide III whose main vibrational features fall in the region 1200–1300 cm^{-1} (these latter primarily attributed to N-H bending coupled with C-N stretching). Variations in these regions are usually associated with protein conformational changes or aggregation linked to cellular stress responses [28]. Additionally, lipid components, identified by ester carbonyl (C=O) stretching bands at around 1744 cm^{-1}, shows an increased trend over time. This assignment aligns with observations in hepatic cell lines where lipid accumulation, such as in steatosis models, shows prominent signals around this wavenumber, often decreasing under certain conditions like differentiation or stress. For instance, research on single-cell Raman spectroscopy in hepatocyte-like cells explicitly links the 1744 cm^{-1} band to lipid carbonyl features, corroborated by triglyceride concentration assays [29]. Raman spectra of lipid droplets of HepG2 cells, treated with fatty acids, confirm similar ester vibrations near 1735–1744 cm^{-1}, distinguishing lipid compositions from proteins. Another study maps total lipids at 1744 cm^{-1} in single cells, reinforcing its lipid specificity across hepatic contexts [30].

Figures 4c,d show the positive correlation between the Amide I band and the gene expressions of *GLUT1, FN1*, and *BBC3*, as well as the positive correlation between the lipid band and *FN1* expression. Conversely, there is a negative correlation between the lipid band and *PCNA* expression. These correlations indicate that the Amide I band is linked to protein-related gene activity, while the lipid band highlights lipid metabolism and membrane

dynamics associated with ECM remodeling. According to literature [30], lipid peroxidation contributes primarily through changes in lipid chain vibrations, visible in Raman spectra at around 1750 cm^{-1} (C=O stretching of ester groups in triacylglycerols) and 1660 cm^{-1} (C=C stretching indicating unsaturated fatty acids like oleic or linoleic). FTIR similarly detects these in the 1700–1750 cm^{-1} region for carbonyl formation and 1260–1300 cm^{-1} for altered C–O and C–H deformations in peroxidized lipids. These bands intensify in HepG2 under fatty acid stress, signaling lipid droplet accumulation and oxidation.

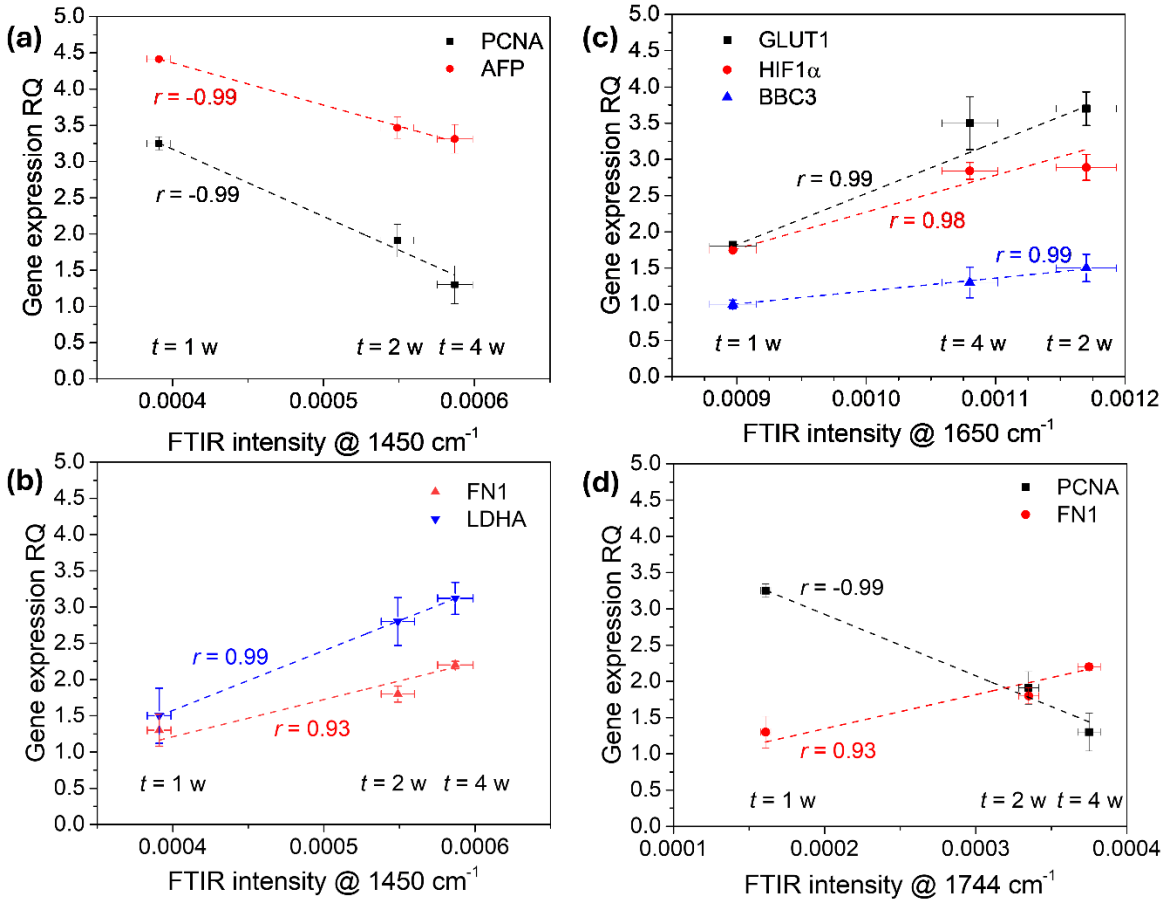

Figure 4. Correlations between ATR-FTIR bands at (**a**) and (**b**) 1450 cm^{-1}, (**c**) 1650 cm^{-1}, (**d**) 1744 cm^{-1} and gene expression for HepG2 3D model acquired at the considered incubation times.

Hence, in our study, changes in lipid band positions or intensities indicate membrane remodeling and lipid peroxidation caused by oxidative stress, which are critical aspects of cellular processes (the cell's physiological state) and the microenvironment. In details, these alterations are linked to membrane lipid synthesis, breakdown, and transport, which play fundamental roles in cellular lipid homeostasis and membrane domain organization essential for cellular signaling and organelle interactions [31–33]. Finally, we outline that ROS features in Raman spectra of apoptotic HepG2 cells appear at key peaks like 1005 cm^{-1} (phenylalanine, protein oxidation), 1445 cm^{-1} (lipid CH_2 deformation linked to ROS-induced changes), and 1655 cm^{-1} (amide I, protein secondary structure alterations). These subtle shifts, rather than major peak displacements, encode ROS dynamics, as captured by advanced models in non-invasive detection. FTIR counterparts include 1650–1660 cm^{-1} (amide I shifts from ROS-protein interactions) and broader 1000–1100 cm^{-1} regions for oxidized biomolecules [34]. The behavior of the IR peaks in the high wavenumber region corroborates the patterns previously identified in the IR peak trends at lower wavenumber. In the 2850–2950 cm^{-1} range, the characteristic symmetric and asymmetric stretching vibrations of methylene groups, namely $–CH_2$ and $–CH_3$, belonging to lipid components, show clear more resolved and intense spectral features, index of a lipid accumulation peculiar of an alteration state in the ECM. Going on, it is worth noting the spectral changes versus incubation time in the region from 3000 to 3800 cm^{-1} primarily associated with O–H and N–H stretching vibrations, ascribed to water, protein secondary structure and hydrogen bonding interactions during the incubation period. Their strong contribution indicates the occurrence of protein misfolding and cellular oxidation. A recent study [35] documented an increase in lipid content in HepG2 cells

under steatotic conditions, linked to stress phenomena and cellular damage. Ultimately, also the vibrational features in the range 2850–2950 cm^{-1} can be used as markers of an altered state of the cell and ECM.

As far as Raman measurements are concerned, Figure 5 shows Raman spectra of the analyzed HepG2 cells after background subtraction and normalization to the total spectral area, ensuring a consistent basis for comparative analysis. As is well known, this approach leverages the inelastic scattering principle of Raman spectroscopy, which captures molecular vibrations specific to chemical bonds and molecular structures, thereby generating a unique "fingerprint" spectrum of cellular constituents including nucleic acids, proteins, and lipids [36].

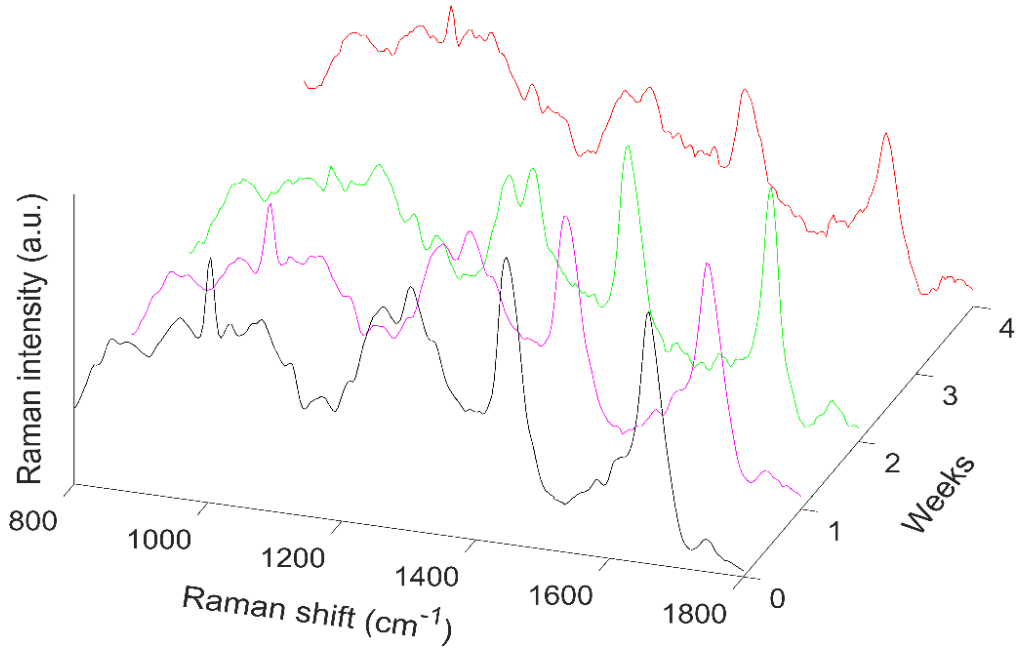

Figure 5. Micro-Raman spectra of HepG2 3D model acquired at the considered incubation times.

The reproducibility of these Raman spectral features, as well as those obtained from ATR-FTIR, across multiple weeks underscores the robustness of these spectroscopic methods for longitudinal studies of 3D HepG2 cell models, from the point of incubation up to 4 weeks. When comparing all Raman profiles, we observe that several spectra cluster closely together yet exhibit subtle differences that reflect dynamic biochemical changes over time. To rigorously dissect these variances while preserving the high-dimensional spectral information, we employed Principal Component Analysis (PCA). PCA is particularly suited here as an unsupervised dimensionality reduction technique: it identifies the principal components capturing the maximum variance across spectra, enabling clear visualization of temporal trajectories, detection of outliers, and discrimination of subtle spectral shifts without prior assumptions about group memberships, essential for monitoring progressive cellular adaptations in this longitudinal setup. As shown in Figure 6, PCA quite clearly resolves distinct temporal patterns in the spectra.

Principal Component Analysis (PCA) of Raman spectra is indispensable for unraveling the complex, multidimensional evolution of the model. PCA reduces spectral noise and variability, extracting principal components that capture the dominant variances, such as shifts in lipid membranes, protein folding, nucleic acid content, and metabolic byproducts, across time points. This enables visualization of temporal trajectories in score plots, revealing clustering patterns that distinguish proliferation phases, extracellular matrix remodeling, and potential oncogenic progression. Without PCA, the high-dimensional spectral data would overwhelm interpretation, obscuring subtle biomarkers of 3D spheroid maturation. However, PCA alone provides a high-level, holistic view; its true power emerges only when paired with detailed, peak-specific analysis of individual Raman bands within the studied spectral interval. This point-by-point dissection is absolutely crucial, far beyond supplementary, for accurate biological interpretation, especially in validating how the 3D HepG2 model recapitulates real epatocarcinoma behavior.

For instance, broad vibrational Raman bands, present also in ATR-FTIR absorbance spectra, are centered at about 1085 cm^{-1} and in the region 1230–1300 cm^{-1}, mainly corresponding to the vibrational modes of nucleic acids and Amide III, respectively, indeed reflecting the cellular genetic material's molecular fingerprint. It is noteworthy that the band centered at about 1265 cm^{-1} is increasingly structured over time showing two different resolved contributions only at t = 4 weeks. These variations of the band suggest the occurrence of protein

conformational changes [37]. Furthermore, the signal at about 1450 cm^{-1} corresponding to vibrational modes present in proteins and lipids, revealing the presence and state of cellular membrane and structural components is well evident in Raman spectra [30]. Raman spectra also prominently feature the Amide I band in ECM structure centered at around 1650 cm^{-1} which strongly decreases at $t = 4$ weeks signaling a decrease in the protein expression due to conformational changes and/or aggregation. Both these two bands show a strong negative correlation with *SPARC* expression (Figure 7a), indicating that these Raman contributions, mainly related to protein secondary structure and conformation, decrease in intensity as *SPARC* expression increases. The growth in *SPARC* expression levels promotes extracellular matrix remodeling and altered protein organization, due to its role in regulating cell–matrix interactions and glycoprotein modulation during tumor progression [38,39]. As shown in Figure 7b, BBC3 expression is initially downregulated compared to 2D monolayer cultures but increases during prolonged cultivation (t = 2 weeks), and then strongly decrease (t = 4weeks), closely to the initial value, reflecting its role in apoptosis regulation within the 3D environment, where the temporal progression of its expression mirrors cellular adaptations (as a decreased DNA/RNA synthesis) related to survival and cell death in the 3D HepG2 system [3,13,14,40].

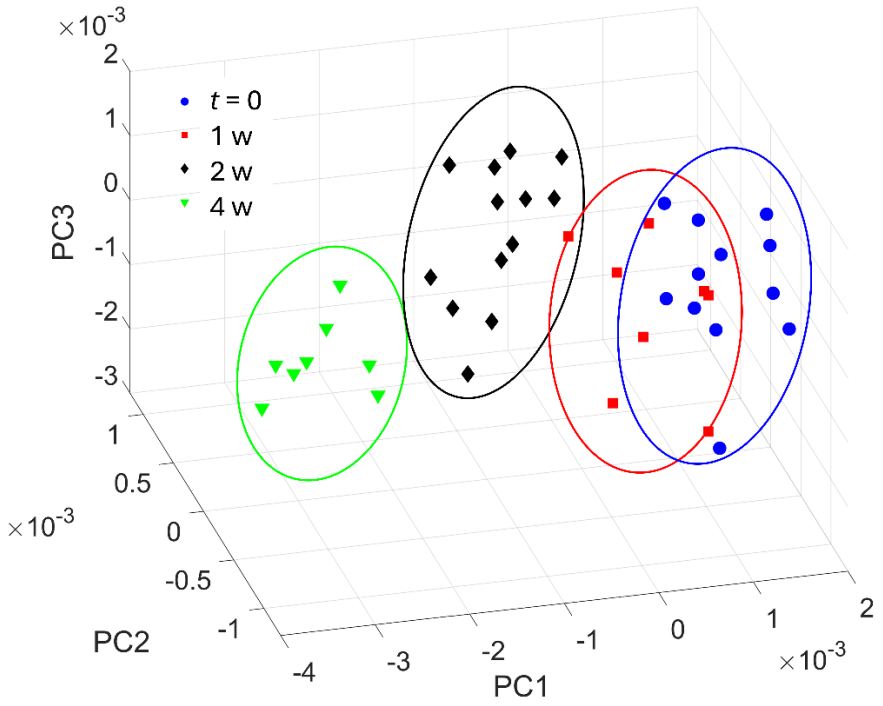

Figure 6. PCA analysis results in terms of the score plot for the three first principal components.

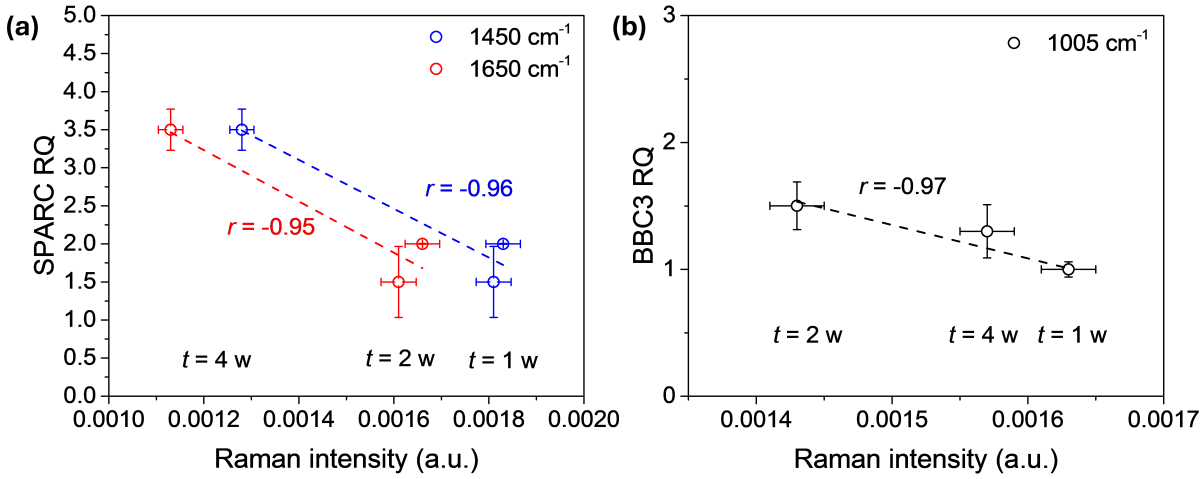

Figure 7. Correlation between (**a**) the Raman bands centered at 1450 and 1650 cm^{-1} with *SPARC* expression and (**b**) centered at 1005 cm^{-1} with *BBC3* expression for HepG2 3D model acquired at the considered incubation times.

Our Raman and ATR-FTIR analyses on the 3D HepG2 model reveal molecular changes consistent with prior studies on HepG2 spheroids and 3D tumor models, particularly in hypoxia-driven adaptations and ECM remodeling.

Specifically, longitudinal spectral shifts in protein bands (e.g., Amide I at ~1650 cm^{-1} and Amide II) align with established Raman/FTIR observations in HepG2 spheroids, where hypoxia stabilizes *HIF1α*, inducing glycolytic shifts and Warburg effect-like metabolism. Increased ATR-FTIR absorbance in protein regions mirrors ECM remodeling via upregulated *SPARC* and *FN1*, as seen in scaffold-free 3D HepG2 models under prolonged hypoxia, reflecting collagen alignment and invasive phenotypes. Raman bands at ~1450 cm^{-1} and ~1080 cm^{-1} correlating negatively with *PCNA/AFP* and positively with *HIF1α/GLUT1/LDHA* match prior characterizations of metabolic quiescence (G0/G1 accumulation) and phospholipid/amide vibrations in maturing HepG2 spheroids [3,13,29,41].

4. Discussion

Complementing the biological insights, Raman and ATR-FTIR spectroscopy analyses uncover molecular and biochemical changes linked to gene expression markers, although not in a perfectly analogous manner. From a physiological perspective, the longitudinal changes observed in vibrational profiles mirror the intrinsic capacity of hepatocellular carcinoma cells to adapt to microenvironmental constraints, such as hypoxia and nutrient deprivation. These conditions drive metabolic rewiring, stress response activation, and extracellular matrix remodeling, which together underpin tumor persistence and progression. To further investigate that by using the spectroscopic techniques, in Figure 8, we compare the ATR-FTIR and Raman profiles on 3D HepG2 model versus the incubation time in the common spectral region 800–1800 cm^{-1}. As can be seen by a first inspection of the figure, some bands in the spectral profiles show an evident overlapping ascribed to the occurrence that the used vibrational spectroscopic techniques reflect both biochemical changes of the investigated samples. However, differences in the spectral behavior of the 3D HepG2 model are evident due to the complementarity of the two techniques. As is well-known, Raman spectroscopy is sensitive to changes in molecular polarizability, while ATR-FTIR absorbance technique is related to variations in the molecule's dipole moment. Therefore, changes in the three-dimensional protein environment (e.g., 3D cellular interactions, hydration, aggregation) can affect the contribution of the bands distinctly in the two techniques.

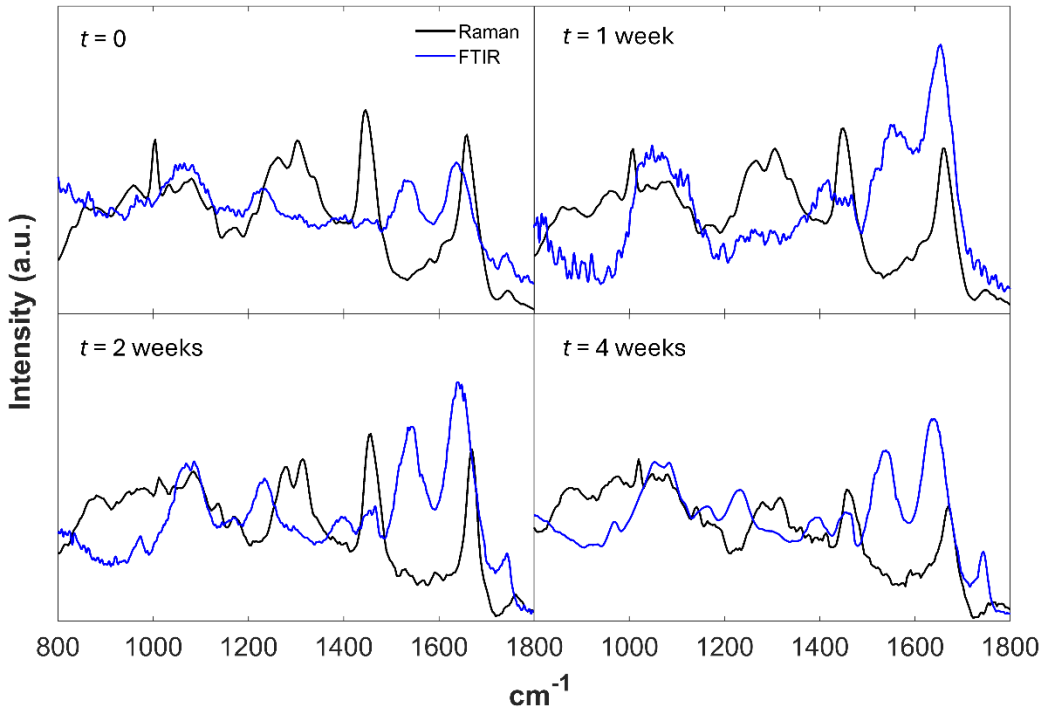

Figure 8. ATR-FTIR and Raman spectra on 3D HepG2 model versus the incubation time in the common spectral region 800–1800 cm^{-1}.

The observed increase of the ATR-FTIR absorbance bands related to proteins corresponds to the enhanced presence of extracellular vesicles (EVs) induced by hypoxia. The features of protein-related bands are observed both in ATR-FTIR and Raman spectra supporting the idea that cancer cells respond to hypoxic stress by producing and modifying EVs, reflecting an adaptive alteration in their extracellular environment. In fact, the evident band centered at about 1650 cm^{-1} in the ATR-FTIR spectra (blue line) of 3D HepG2 cells model, increases over time up to two weeks suggesting an enhanced content or a higher degree of organization of the protein secondary structures in the Amide I structure in accordance with ongoing extracellular matrix (ECM) remodeling. At the

same time, the simultaneous decrease in the overlapped Raman contribution (black line) could be due to differences in the selectivity or sensitivity of the two spectroscopic techniques towards certain molecular vibrations or to conformational or environmental changes of the proteins that influence the Raman signals differently than the ATR-FTIR ones, as above evidenced. According to these evidences, ATR-FTIR and micro-Raman spectroscopies can be proposed as a diagnostic tool in the speeding up of cell status identification, assessing the intracellular biochemical changes that take place in cancer cells; particularly, analyzing hypoxia-ascribed vibrational features will help to better understand tumor progression, resistance mechanisms, and potential therapeutic targets.

Physiologically, tumor hypoxia leads to the adaptation of cancer cells to survive in an oxygen-deprived environment, which influences their metabolism, growth, and behavior. The spectroscopic evidence of protein and lipid remodeling, together with gene expression changes, is consistent with *HIF1α* stabilization and the induction of glycolytic metabolism, in line with the Warburg effect, a hallmark of tumor physiology. This condition triggers signaling pathways that promote angiogenesis, such as the stabilization of hypoxia-inducible factors (*HIFs*), which regulate genes involved in oxygen delivery and energy metabolism. These mechanisms include the activation of cellular processes that enhance survival under stress, such as increased autophagy and alteration of cell cycle checkpoints. In a 3D HepG2 model, the altered extracellular matrix (ECM) composition strongly influences the molecular profile and can promote more resistant and adaptive cellular phenotypes. In our previous study [13], we have shown that hypoxia-driven ECM remodeling leads to increased expression of *SPARC*. Thus, it is interesting to follow the spectroscopic features ascribed to the *SPARC* expression. In the previous section, we have already described its correlation with Raman bands centered at 1450 and 1650 cm^{-1} (Figure 7a) reflecting changes in protein conformation linked to the modulation of cell–matrix interactions and glycoproteins over time. In addition, glycoproteins typically contribute to absorption features principally in the 1000–1200 cm^{-1} range, mainly due to C–O–C and C–O stretching vibrations. Notably, the band splitting detected in ATR-FTIR spectra at 4 weeks within this region indicates spatial and conformational heterogeneity in glycoproteins. Such heterogeneity may result from alterations in glycosylation patterns or molecular interactions shaped by the 3D tumor architecture and hypoxic microenvironment.

On the overall, the progressive rise of *SPARC* values and the corresponding spectroscopic changes, reflect an active ECM remodeling program. This is a crucial physiopathological process that not only provides structural support but also modulates cell–matrix signaling, promoting invasion and metastatic competence. Specifically, the changes in the ATR-FTIR spectra after several weeks include alterations in the Amide I and Amide II bands, reflecting protein conformational changes linked to *HIF1α* activation and increased expression (Figure 4). In addition, the variations in lipid and carbohydrate spectral regions suggest metabolic shifts, such as enhanced glycolysis and changes in membrane composition. All that variations are associated with metabolic reprogramming during prolonged hypoxia consistent with increased cell proliferation and hypoxia-driven metabolic remodeling [42–47]. FTIR peaks changes are in good agreement with those of the broad Raman band centered at about 1080 cm^{-1}. This latter band, linked to phospholipid and amide-related molecular vibrations, negatively correlates with *PCNA* and *AFP* expression (Figure 9a,c) and positively with *HIF1α, GLUT1,* and *LDHA* (Figure 9b,d). The critical interplay between hypoxia and ECM remodeling in tumor progression is also confirmed by the trends vs. *FN1* in the case of ATR-FTIR and BBC3 for Raman: hypoxia-inducible factor (*HIF*) activation drives metabolic reprogramming and induces ECM components like *SPARC*, fostering a microenvironment conducive to cancer cell survival and dissemination [48–51]. All these observations are coherent with literature data reporting the already mentioned lipid peroxidation caused by oxidative stress and reflected by the progressive enhancements of Raman bands at around 1750 and 1660 cm^{-1} [30] and FTIR ones in the 1700–1750 and 1260–1300 cm^{-1} regions [34]. All that together with the occurrence of proteins oxidation and their structural alterations which is indicated by the spectral modifications in the 1650–1660 cm^{-1} and 1000–1100 cm^{-1} regions [3,52,53] On the overall, the ability to access ROS dynamics by looking at specific vibrational modes and at their evolution with time renders our analysis particularly important to follow the 3D model tumor progression.

Ultimately, our approach based on the complementary use of ATR-FTIR and Raman highlights technique-specific sensitivities (e.g., dipole vs. polarizability changes), revealing distinct responses in overlapping 800–1800 cm^{-1} regions, such as decreasing Raman at 1650 cm^{-1} despite rising ATR-FTIR amid EV production, unexplored in prior single-technique HepG2 studies. Band splitting in glycoproteins (1000–1200 cm^{-1}) at 4 weeks indicates hypoxia-shaped glycosylation heterogeneity in 3D architecture, extending beyond general ECM trends in earlier models. Correlations of ~1080 cm^{-1} Raman band with *BBC3* (apoptosis) and *FN1* trends versus incubation time offer new real-time spectroscopic proxies for resistance mechanisms, advancing diagnostic potential over static 2D/3D comparisons.

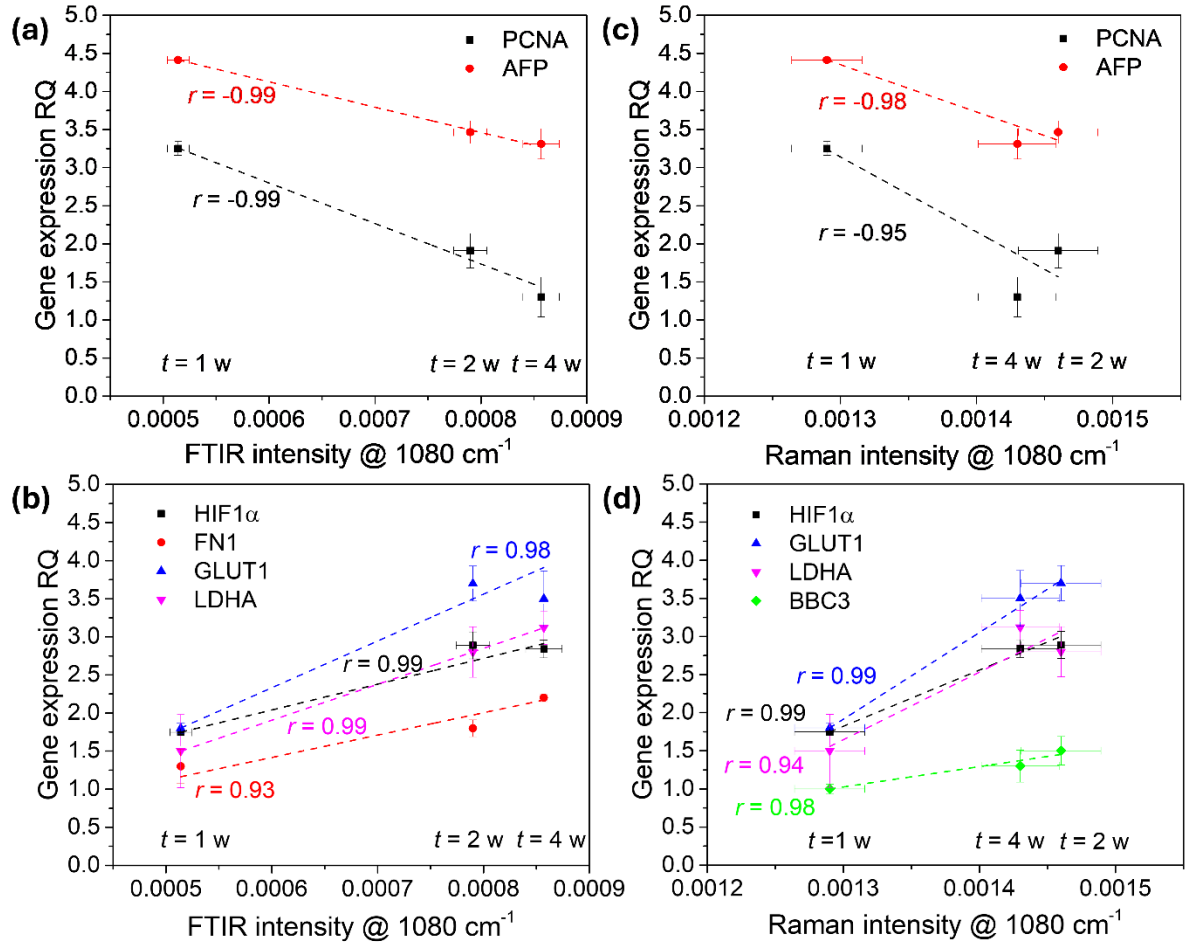

Figure 9. Correlation between ATR-FTIR (**a**,**b**) and Raman (**c**,**d**) band centered at about 1080 cm^{-1} with gene expressions for HepG2 3D model acquired at the considered incubation times. PCNA and AFP (**a**,**c**); HIF1a, FN1, GLUT1 and LDHA (**b**); HIF1a, GLUT1, LDHA and BBC3 (**d**).

5. Conclusions

The combination of ATR-FTIR absorbance and Raman scattering has proven to be an invaluable tool for monitoring intrinsic molecular signatures of cells over time, reflecting cellular phenotype, metabolic state, and adaptive responses in hepatocellular carcinoma (mimicked here by a 3D HepG2 model), including hypoxia-driven metabolic reprogramming and extracellular matrix remodeling, without invasive procedures or fluorescent tagging. Gene expression analysis revealed an early proliferative phase marked by upregulation of *PCNA*, *KI-67*, and *AFP*, followed by activation of hypoxia- and stress-associated pathways (*HIF1α*, *SLC2A1/GLUT1*, *LDHA*) and modulation of ECM components (*SPARC*, *FN1*) alongside the pro-apoptotic regulator *BBC3*. In parallel, Raman and ATR-FTIR spectroscopies non-invasively detected biochemical variations related to oxidative stress, lipid accumulation, apoptosis, and ECM remodeling, with strong correlations between spectral signatures and these molecular markers demonstrating the reliability of label-free spectroscopic fingerprints as indicators of physiopathological processes. The good correlation between ATR-FTIR/Raman spectral bands and gene expression underscores the interpretative power of vibrational techniques beyond phenomenological observations. By integrating molecular spectroscopy with transcriptomics, this study offers an innovative approach for tracking tumor evolution and microenvironment-induced phenotypic modulation in 3D cell models.

Author Contributions

E.F.: Conceptualization, Investigation, Data curation, Writing—review & editing. C.C.: Investigation, Visualization, Data curation, Writing—review & editing. V.C.: Data curation, Writing—review & editing. S.C.: Supervision—review & editing. F.N.: Supervision—review & editing. M.G.R.: Conceptualization, Resources, Writing—review & editing.

Funding

This work has been partially funded by European Union (NextGeneration EU), through the MUR-PNRR project SAMOTHRACE(ECS00000022).

Institutional Review Board Statement

Not applicable.

Informed Consent Statement

Not applicable.

Data Availability Statement

Data are available from the corresponding author on reasonable request.

Conflicts of Interest

The authors declare no conflict of interest.

Use of AI and AI-Assisted Technologies

No AI tools were utilized for this paper.

References

1. Zhu, L.; Cheng, C.; Liu, S.; et al. Advancements and Application Prospects of Three-Dimensional Models for Primary Liver Cancer: A Comprehensive Review. *Front. Bioeng. Biotechnol.* **2023**, *11*, 1343177. https://doi.org/10.3389/fbioe.2023.1343177.
2. Pastore, M.; Giachi, A.; Spínola-Lasso, E.; et al. Organoids and Spheroids: Advanced in Vitro Models for Liver Cancer Research. *Front. Cell Dev. Biol.* **2025**, *12*, 1536854. https://doi.org/10.3389/fcell.2024.1536854.
3. Štampar, M.; Breznik, B.; Filipič, M.; et al. Characterization of In Vitro 3D Cell Model Developed from Human Hepatocellular Carcinoma (HepG2) Cell Line. *Cells* **2020**, *9*, 2557. https://doi.org/10.3390/cells9122557.
4. Monaghan, J.F.; Byrne, H.J.; Lyng, F.M.; et al. Radiobiological Applications of Vibrational Spectroscopy: A Review of Analyses of Ionising Radiation Effects in Biology and Medicine. *Radiation* **2024**, *4*, 276–308. https://doi.org/10.3390/radiation4030022.
5. Allakhverdiev, E.S.; Kossalbayev, B.D.; Sadvakasova, A.K.; et al. Spectral Insights: Navigating the Frontiers of Biomedical and Microbiological Exploration with Raman Spectroscopy. *J. Photochem. Photobiol. B* **2024**, *252*, 112870. https://doi.org/10.1016/j.jphotobiol.2024.112870.
6. Vu, K.H.P.; Blankenburg, G.H.; Lesser-Rojas, L.; et al. Applications of Single-Molecule Vibrational Spectroscopic Techniques for the Structural Investigation of Amyloid Oligomers. *Molecules* **2022**, *27*, 6448. https://doi.org/10.3390/molecules27196448.
7. Rizzo, M.G.; Yadav, N.; Morganti, D.; et al. 3D MicroOrganoSpheres Formation of Hepatocellular Carcinoma on Chip as a Novel in Vitro Model for Physiological and Therapeutic Studies. In *Sensors and Microsystems*; Sabrina, C., Corrado, D.N., Luca, P., et al, Eds.; Springer Nature: Cham, Switzerland, 2025; pp. 9–18.
8. Rizzo, M.G.; Morganti, D.; Smeriglio, A.; et al. Formation of 3D Human Osteoblast Spheroids Incorporating Extracellular Matrix-Mimetic Phage Peptides as a Surrogate Bone Tissue Model. *Int. J. Mol. Sci.* **2025**, *26*, 8482. https://doi.org/10.3390/ijms26178482.
9. Rizzo, M.G.; Cordaro, M.; Morganti, D.; et al. Osteogenic Activity and Bone Matrix Mineralization Induced by *Vitis Vinifera* Leaves Extract in Human Osteoblastic Cells. *Food Sci. Nutr.* **2025**, *13*, e70785. https://doi.org/10.1002/fsn3.70785.
10. Chaudhary, I.; Jackson, N.; Denning, D.; et al. Contributions of Vibrational Spectroscopy to Virology: A Review. *Clin. Spectrosc.* **2022**, *4*, 100022. https://doi.org/10.1016/j.clispe.2022.100022.
11. Zhang, S.; Qi, Y.; Tan, S.P.H.; et al. Molecular Fingerprint Detection Using Raman and Infrared Spectroscopy Technologies for Cancer Detection: A Progress Review. *Biosensors* **2023**, *13*, 557. https://doi.org/10.3390/bios13050557.
12. Siddhanta, S.; Kuzmin, A.N.; Pliss, A.; et al. Advances in Raman Spectroscopy and Imaging for Biomedical Research. *Adv. Opt. Photonics* **2023**, *15*, 318. https://doi.org/10.1364/AOP.479884.
13. Rizzo, M.G.; Fazio, E.; De Pasquale, C.; et al. Physiopathological Features in a Three-Dimensional In Vitro Model of Hepatocellular Carcinoma: Hypoxia-Driven Oxidative Stress and ECM Remodeling. *Cancers* **2025**, *17*, 3082. https://doi.org/10.3390/cancers17183082.

14. Rizzo, M.G.; Corsaro, C.; Marrara, S.; et al. Raman Spectral Analyses to Investigate the Physiological and Metabolic Development of a 3D Hepatocellular Carcinoma Model. *Spectrochim. Acta A Mol. Biomol. Spectrosc.* **2025**, *343*, 126564. https://doi.org/10.1016/j.saa.2025.126564.
15. Takahashi, Y.; Hori, Y.; Yamamoto, T.; et al. 3D Spheroid Cultures Improve the Metabolic Gene Expression Profiles of HepaRG Cells. *Biosci. Rep.* **2015**, *35*, e00208. https://doi.org/10.1042/BSR20150034.
16. Sae-be, A.; Wiwatpanit, T.; Varatthan, T.; et al. Comparative Study between the 3D-Liver Spheroid Models Developed from HepG2 and Immortalized Hepatocyte-Like Cells with Primary Hepatic Stellate Coculture for Drug Metabolism Analysis and Anticancer Drug Screening. *Adv. Ther.* **2023**, *6*, 2200169. https://doi.org/10.1002/adtp.202200169.
17. Gao, J.; Senthil, M.; Ren, B.; et al. IRF-1 Transcriptionally Upregulates PUMA, Which Mediates the Mitochondrial Apoptotic Pathway in IRF-1-Induced Apoptosis in Cancer Cells. *Cell Death Differ.* **2010**, *17*, 699–709. https://doi.org/10.1038/cdd.2009.156.
18. Apicella, C.; Ruano, C.S.M.; Jacques, S.; et al. Urothelial Cancer Associated 1 (UCA1) and MiR-193 Are Two Non-Coding RNAs Involved in Trophoblast Fusion and Placental Diseases. *Front. Cell Dev. Biol.* **2021**, *9*, 633937. https://doi.org/10.3389/fcell.2021.633937.
19. Zhu, C.; Fang, X.; Liu, X.; et al. Squalene Monooxygenase Facilitates Bladder Cancer Development in Part by Regulating PCNA. *Biochim. Biophys. Acta BBA Mol. Cell Res.* **2024**, *1871*, 119681. https://doi.org/10.1016/j.bbamcr.2024.119681.
20. Huang, S.-W.; Kao, J.-K.; Wu, C.-Y.; et al. Targeting Aerobic Glycolysis and HIF-1α Expression Enhance Imiquimod-Induced Apoptosis in Cancer Cells. *Oncotarget* **2014**, *5*, 1363–1381. https://doi.org/10.18632/oncotarget.1734.
21. Franco, D.; Leonardi, A.A.; Rizzo, M.G.; et al. Biological Response Evaluation of Human Fetal Osteoblast Cells and Bacterial Cells on Fractal Silver Dendrites for Bone Tissue Engineering. *Nanomaterials* **2023**, *13*, 1107. https://doi.org/10.3390/nano13061107.
22. Ghimire, H.; Garlapati, C.; Janssen, E.A.M.; et al. Protein Conformational Changes in Breast Cancer Sera Using Infrared Spectroscopic Analysis. *Cancers* **2020**, *12*, 1708. https://doi.org/10.3390/cancers12071708.
23. Butler, M.; Salem, N.; Hoss, W.; et al. Raman Spectral Analysis of the 1300 Cm−1 Region for Lipid and Membrane Studies. *Chem. Phys. Lipids* **1979**, *24*, 99–102. https://doi.org/10.1016/0009-3084(79)90099-9.
24. Ami, D.; Bovio, F.; Forcella, M.; et al. Identifying Label-Free and Untargeted Biomarkers of SH-SY5Y Cell Fate in ATRA-Induced Differentiation through FTIR Spectroscopy and Integrated Omics. *Talanta* **2026**, *296*, 128464. https://doi.org/10.1016/j.talanta.2025.128464.
25. Al-Kelani, M.; Buthelezi, N. Advancements in Medical Research: Exploring Fourier Transform Infrared (FTIR) Spectroscopy for Tissue, Cell, and Hair Sample Analysis. *Skin. Res. Technol.* **2024**, *30*, e13733. https://doi.org/10.1111/srt.13733.
26. Sandt, C.; Nadaradjane, C.; Richards, R.; et al. Use of Infrared Microspectroscopy to Elucidate a Specific Chemical Signature Associated with Hypoxia Levels Found in Glioblastoma. *Analyst* **2016**, *141*, 870–883. https://doi.org/10.1039/C5AN02112J.
27. Cao, R.; Zhao, X.; Li, S.; et al. Hypoxia Induces Dysregulation of Lipid Metabolism in HepG2 Cells via Activation of HIF-2a. *Cell. Physiol. Biochem.* **2014**, *34*, 1427–1441. https://doi.org/10.1159/000366348.
28. Chrabaszcz, K.; Kaminska, K.; Augustyniak, K.; et al. Tracking Extracellular Matrix Remodeling in Lungs Induced by Breast Cancer Metastasis. Fourier Transform Infrared Spectroscopic Studies. *Molecules* **2020**, *25*, 236. https://doi.org/10.3390/molecules25010236.
29. Ma, C.; Zhang, L.; He, T.; et al. Single Cell Raman Spectroscopy to Identify Different Stages of Proliferating Human Hepatocytes for Cell Therapy. *Stem Cell Res. Ther.* **2021**, *12*, 555. https://doi.org/10.1186/s13287-021-02619-9.
30. Paramitha, P.N.; Zakaria, R.; Maryani, A.; et al. Raman Study on Lipid Droplets in Hepatic Cells Co-Cultured with Fatty Acids. *Int. J. Mol. Sci.* **2021**, *22*, 7378. https://doi.org/10.3390/ijms22147378.
31. Rak, S.; De Zan, T.; Stefulj, J.; et al. FTIR Spectroscopy Reveals Lipid Droplets in Drug Resistant Laryngeal Carcinoma Cells through Detection of Increased Ester Vibrational Bands Intensity. *Analyst* **2014**, *139*, 3407–3415. https://doi.org/10.1039/C4AN00412D.
32. Wu, B.-B.; Gong, Y.-P.; Wu, X.-H.; et al. Fourier Transform Infrared Spectroscopy for the Distinction of MCF-7 Cells Treated with Different Concentrations of 5-Fluorouracil. *J. Transl. Med.* **2015**, *13*, 108. https://doi.org/10.1186/s12967-015-0468-2.
33. Xu, J.; Huang, X. Lipid Metabolism at Membrane Contacts: Dynamics and Functions Beyond Lipid Homeostasis. *Front. Cell Dev. Biol.* **2020**, *8*, 615856. https://doi.org/10.3389/fcell.2020.615856.
34. Zhang, C.; Liu, S.; Wan, J.; et al. In-Situ Non-Invasive Detection of Cellular Reactive Oxygen Species by Integrating Raman Spectrum and Bidirectional Gated Recurrent Unit Models. *Biomed. Opt. Express* **2025**, *16*, 4541. https://doi.org/10.1364/BOE.560107.

35. Campos-Espinosa, A.; Guzmán, C.; Medina-Ávila, K.Z.; et al. In Vitro Lipid Overload Affects Cellular Proliferation, Apoptosis, and Senescence in a Time-Dependent Manner in HepG2 Hepatocytes and LX-2 Hepatic Stellate Cells. *Cells* **2024**, *13*, 282. https://doi.org/10.3390/cells13030282.
36. Bonsignore, M.; Trusso, S.; De Pasquale, C.; et al. A Multivariate Analysis of Multiple Myeloma Subtype Plasma Cells. *Spectrochim. Acta A Mol. Biomol. Spectrosc.* **2021**, *258*, 119813. https://doi.org/10.1016/j.saa.2021.119813.
37. Lin, J.; Ruan, Q.; Liao, F.; et al. Characterization of Secreted Proteins in $HepG_2$ and LO_2 Cells by Raman Spectroscopy. In *Optics in Health Care and Biomedical Optics VI*; Luo, Q., Li, X., Gu, Y., et al., Eds.; SPIE: Bellingham, WA, USA, 2014; p. 92682M.
38. Bradshaw, A.D. Diverse Biological Functions of the SPARC Family of Proteins. *Int. J. Biochem. Cell Biol.* **2012**, *44*, 480–488. https://doi.org/10.1016/j.biocel.2011.12.021.
39. Said, N. Roles of SPARC in Urothelial Carcinogenesis, Progression and Metastasis. *Oncotarget* **2016**, *7*, 67574–67585. https://doi.org/10.18632/oncotarget.11590.
40. Roos, W.P.; Kaina, B. DNA Damage-Induced Cell Death by Apoptosis. *Trends Mol. Med.* **2006**, *12*, 440–450. https://doi.org/10.1016/j.molmed.2006.07.007.
41. Pridgeon, C.S.; Airavaara, K.; Monola, J.; et al. Chronic Hypoxia for the Adaptation of Extracellular Vesicle Phenotype. *Sci. Rep.* **2024**, *14*, 25189. https://doi.org/10.1038/s41598-024-73453-1.
42. Shchulkin, A.V.; Abalenikhina, Y.V.; Kosmachevskaya, O.V.; et al. Regulation of P-Glycoprotein during Oxidative Stress. *Antioxidants* **2024**, *13*, 215. https://doi.org/10.3390/antiox13020215.
43. Liang, X.; Weng, J.; You, Z.; et al. Oxidative Stress in Cancer: From Tumor and Microenvironment Remodeling to Therapeutic Frontiers. *Mol. Cancer* **2025**, *24*, 219. https://doi.org/10.1186/s12943-025-02375-x.
44. Luo, Q.; Wang, Q.; Shi, J.; et al. PUMA Reduces FASN Ubiquitination to Promote Lipid Accumulation and Tumor Progression in Human Clear Cell Renal Cell Carcinoma. *Cell Death Dis.* **2025**, *16*, 460. https://doi.org/10.1038/s41419-025-07782-y.
45. Ferrer, C.M.; Lynch, T.P.; Sodi, V.L.; et al. O-GlcNAcylation Regulates Cancer Metabolism and Survival Stress Signaling via Regulation of the HIF-1 Pathway. *Mol. Cell* **2014**, *54*, 820–831. https://doi.org/10.1016/j.molcel.2014.04.026.
46. Spada, S.; Tocci, A.; Di Modugno, F.; et al. Fibronectin as a Multiregulatory Molecule Crucial in Tumor Matrisome: From Structural and Functional Features to Clinical Practice in Oncology. *J. Exp. Clin. Cancer Res.* **2021**, *40*, 102. https://doi.org/10.1186/s13046-021-01908-8.
47. Wicks, E.E.; Semenza, G.L. Hypoxia-Inducible Factors: Cancer Progression and Clinical Translation. *J. Clin. Investig.* **2022**, *132*, e159839. https://doi.org/10.1172/JCI159839.
48. Nowak-Stępniowska, A.; Osuchowska, P.N.; Fiedorowicz, H.; et al. Hypoxia-Induced Extracellular Matrix Deposition in Human Mesenchymal Stem Cells: Insights from Atomic Force, Scanning Electron, and Confocal Laser Microscopy. *Appl. Sci.* **2025**, *15*, 10701. https://doi.org/10.3390/app151910701.
49. Gilkes, D.M.; Semenza, G.L.; Wirtz, D. Hypoxia and the Extracellular Matrix: Drivers of Tumour Metastasis. *Nat. Rev. Cancer* **2014**, *14*, 430–439. https://doi.org/10.1038/nrc3726.
50. Magar, A.G.; Morya, V.K.; Kwak, M.K.; et al. A Molecular Perspective on HIF-1α and Angiogenic Stimulator Networks and Their Role in Solid Tumors: An Update. *Int. J. Mol. Sci.* **2024**, *25*, 3313. https://doi.org/10.3390/ijms25063313.
51. Yuan, Z.; Li, Y.; Zhang, S.; et al. Extracellular Matrix Remodeling in Tumor Progression and Immune Escape: From Mechanisms to Treatments. *Mol. Cancer* **2023**, *22*, 48. https://doi.org/10.1186/s12943-023-01744-8.
52. Junhom, C.; Weerapreeyakul, N.; Tanthanuch, W.; et al. FTIR Microspectroscopy Defines Early Drug Resistant Human Hepatocellular Carcinoma (HepG2) Cells. *Exp. Cell Res.* **2016**, *340*, 71–80. https://doi.org/10.1016/j.yexcr.2015.12.007.
53. Maurotti, S.; Scopacasa, B.; Scionti, F.; et al. Raman Spectroscopic Characterization of Liver Steatosis and Fibrosis in a 2D and 3D in Vitro Thyroxine-Treated Hypothyroid Cellular Model. *Mol. Cell Endocrinol.* **2026**, *611*, 112679. https://doi.org/10.1016/j.mce.2025.112679.